Complete Imaging of Transcrustal Magmatic Systems with TomoATT, SurfATT, and PmPNet

P. Tong[1,2], T. Li[1], J. Chen[1], S. Hao[1], M. Xu[1,3], G. Chen[1], M. Nagaso[1], and the team

1. Division of Mathematical Sciences, School of Physical and Mathematical Sciences, Nanyang Technological University, Singapore

2. Earth Observatory of Singapore, Nanyang Technological University, Singapore

I. Seismic Imaging of Transcrustal Magmatic Systems beneath Volcanoes

Transcrustal Magmatic Systems

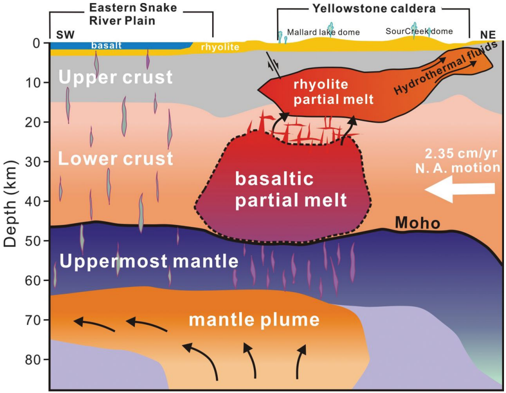

Definition

Transcrustal Magmatic Systems (TMS) refer to vertically connected networks of magma storage, transport, and accumulation zones that extend from the mantle through the lower crust, mid-crust, and up to shallow crustal reservoirs beneath volcanoes.

Image credit: Hsin-Hua Huang, University of Utah.

Transcrustal Magmatic Systems

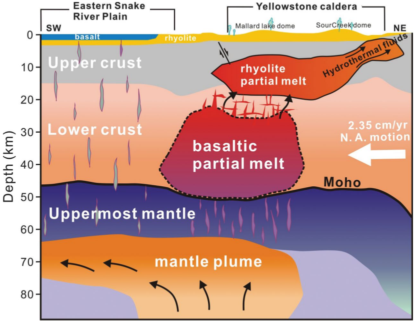

Key features

- Multi-level magma storage: Instead of one large chamber, magma resides in several smaller reservoirs or mush zones at different depths. Much of the system consists of partially molten "mush," not large liquid pools (Crystal–melt mush zones).
- Dynamic connections: Magma moves episodically between levels, feeding eruptions or stalling at depth. These systems can persist for tens of thousands to millions of years.

Image credit: Hsin-Hua Huang, University of Utah.

Transcrustal Magmatic Systems

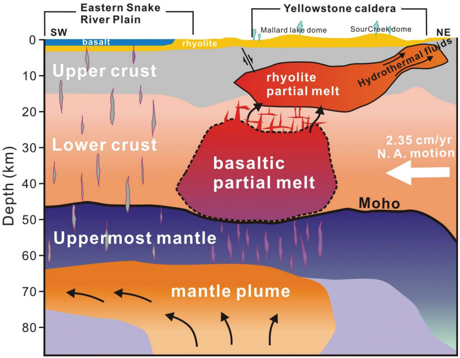

Why they matter

- They help explain how volcanoes are fed, how eruptions are triggered, and why magma compositions are diverse.
- They modify crustal structure and are important for understanding mineralization, thermal evolution, and geodynamic processes.
- They challenge the old idea of a single large magma chamber.

Transcrustal Magmatic Systems

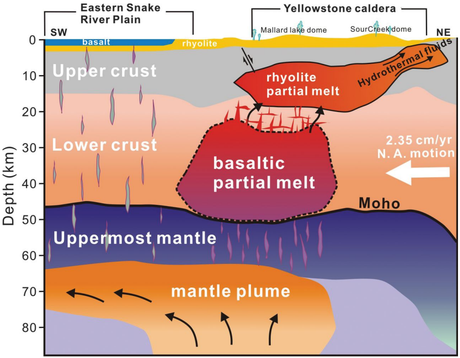

Typical components

- Mantle melt source
- Lower crustal hot zones (LCHZ)
- Mid-crustal reservoirs / mush zones
- Upper-crustal chambers
- Dikes, sills, conduits connecting the entire system

Primary Motivation: Geothermal Energy Exploration

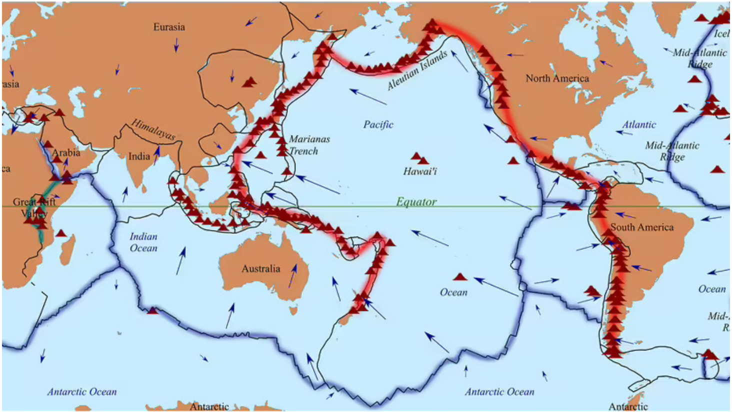

The Ring of Fire: Geothermal Plants Cluster in Volcanic Regions

California: Geothermal Plants Cluster in Volcanic Regions

Geothermal Energy Potential in Singapore

- A two-year, SGD 16 million contract was awarded to Surbana Jurong in September 2024 to assess Singapore's geothermal potential using geophysical methods.
- Ongoing discussion on the potential risk of induced seismicity due to the development of geothermal power plants in Singapore.

Seismic Imaging of Transcrustal Magmatic Systems

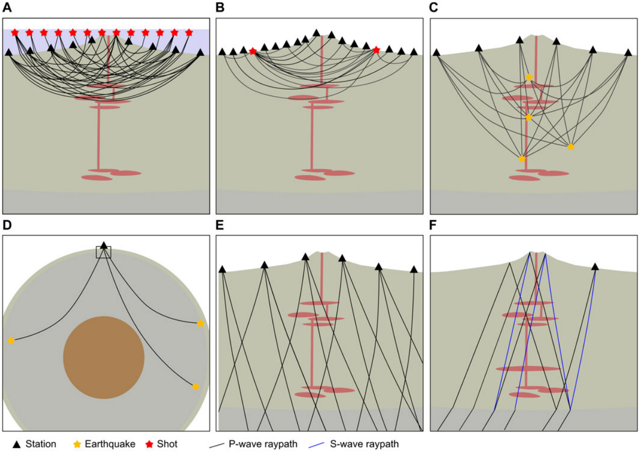

Commonly used seismic data: (1) Active sources. (2) Local and/or regional earthquakes. (3) Teleseismic events. (4) Ambient noise.

Image credit: Paulatto et. al., Front. Earth Sci., 2022.

II. Seismic Imaging Software: TomoATT & SurfATT

Software: Adjoint-state traveltime tomography

- Body wave tomography

TomoATT

- Surface wave tomography

SurfATT

Adjoint-state Traveltime Tomography

A new comprehensive framework for

A. Body Wave Tomography
   - Velocity Heterogeneity: Vp, Vs Tong, JGR, 2021a; Chen et al., JGR, 2023; Tong et al., GJI, 2024
   - Anisotropy Tomography
     Tong, JGR, 2021b; Wu et al., GRL, 2022; Wang et al., JGR, 2022; Chen et al., GJI, 2023.
   - Attenuation Tomography Wang et al., JGR, 2025.
   - Reflection Tomography Chen et al., JGR, 2025.

B. Surface Wave Tomography
   - Topography-incorporated ambient noise tomography for velocity heterogeneity Hao et al., JGR: Solid Earth, 2024.
   - Topography-incorporated ambient noise tomography for velocity heterogeneity and seismic anisotropy Hao et al., submitted.

C. Earthquake Location Tong et al., GJI, 2024

Seismic Data: Active sources for near surface imaging

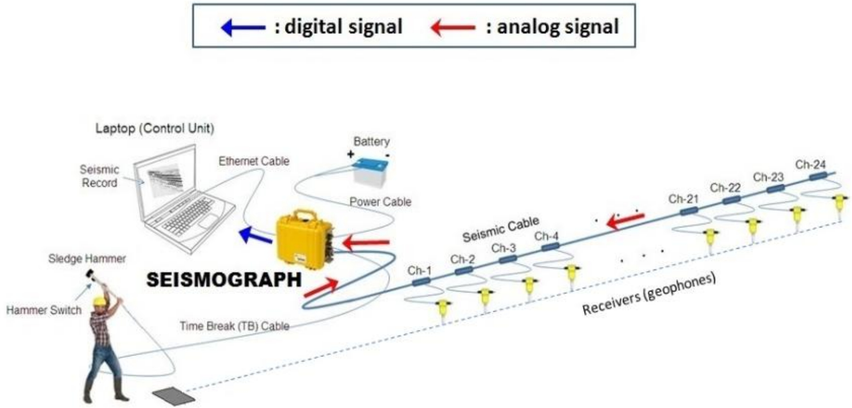

Courtesy of https://www.parkseismic.com

Seismic Data: Absolute arrival times of natural earthquakes

Northeast Japan, Bandpass Filter: 5 s - 10 s

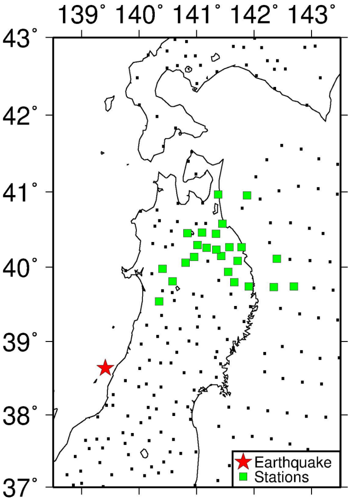

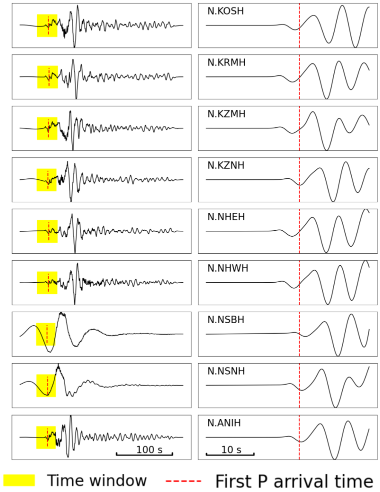

Seismic Data: Common-source differential arrival times

P-waves: Cross-correlation Traveltime Measurements

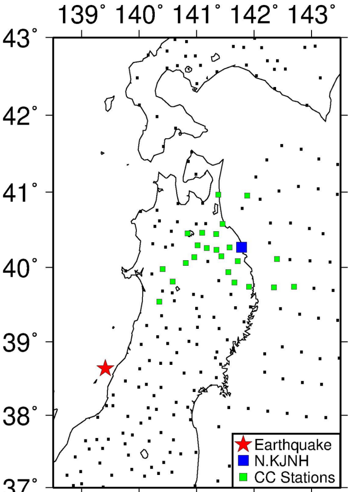

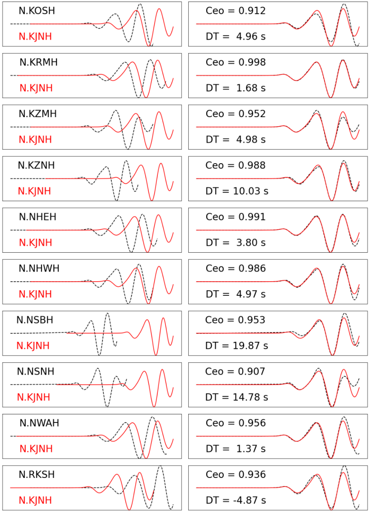

Seismic Data: Ambient Noise

Ambient noise from environmental and human activities

Why Adjoint-state Traveltime Tomography (ATT)?

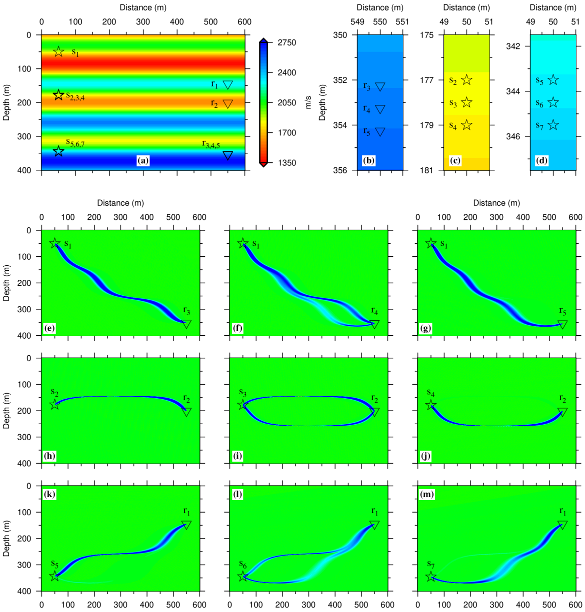

Accuracy and Reliability

- Eikonal equation is utilized to model traveltime.
- No ray tracing is required.
- Dealing with the multipath problem properly.

Computational Efficiency

- Eikonal equation $T(x, y, z)$
- Wave equation $\mathbf{u}(t, x, y, z)$
- At least one-order computationally cheaper than solving wave equations

Surface Waves

Topography-incorporated eikonal equation for surface waves (Isotropic):

$$M(\mathbf{x}) = \frac{1}{s^2(\mathbf{x})} \begin{bmatrix} a(\mathbf{x}) & -c(\mathbf{x}) \\ -c(\mathbf{x}) & b(\mathbf{x}) \end{bmatrix} \tag{1}$$

Topography-incorporated eikonal equation for surface waves (Azimuthally anisotropic):

$$\begin{aligned} &M(\mathbf{x}) \\ =&\frac{1}{s^2(\mathbf{x})} \begin{bmatrix} a(\mathbf{x}) & -c(\mathbf{x}) \\ -c(\mathbf{x}) & b(\mathbf{x}) \end{bmatrix} \begin{bmatrix} 1+2\xi(\mathbf{x}) & 2\eta(\mathbf{x}) \\ 2\eta(\mathbf{x}) & 1-2\xi(\mathbf{x}) \end{bmatrix} \begin{bmatrix} a(\mathbf{x}) & -c(\mathbf{x}) \\ -c(\mathbf{x}) & b(\mathbf{x}) \end{bmatrix} \end{aligned} \tag{2}$$

Surface Waves

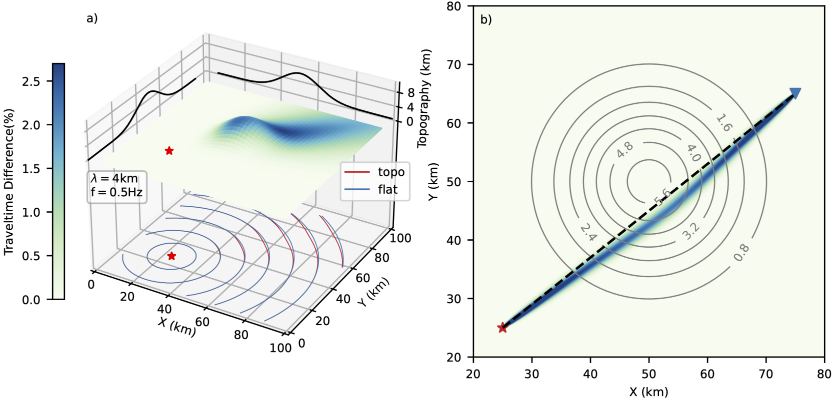

Software: TomoATT

TomoATT

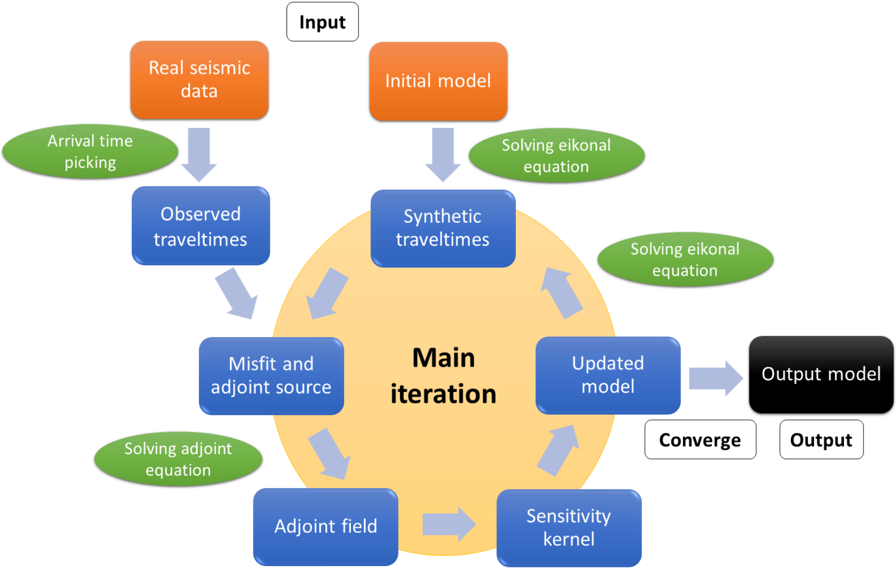
Input
Real seismic data
Initial model
Arrival time picking
Solving eikonal equation
Observed traveltimes
Synthetic traveltimes
Solving eikonal equation
Misfit and adjoint source
Main iteration
Updated model
Output model
Converge
Output
Solving adjoint equation
Adjoint field
Sensitivity kernel

TomoATT

```
0 2013 10  6  9 20 53.00   -1.7673   -0.6619    9.5500  2.66       6 494990 1.0000
0      0   CI_NJQ   -1.0351   -0.3383    219.0000 P   14.761
0      1  CI_GATR   -0.8854   -0.5611    590.0000 P   16.507
0      2   NC_PTQ   -0.8306   -0.5975    448.0000 P   17.127
0      3   CI_FIG   -0.9440   -0.1066    945.0000 P   18.376
0      4   CI_LCP   -0.8184   -0.3112    199.0000 P   19.047
0      5   CI_WGR   -1.4228    0.2975    554.0000 P   18.476
1 1997  1 10 16  5 12.11   -1.7780   -0.6512    5.3600  2.88       5 261963 1.0000
1      0   CI_SSC   -1.7250   -0.2158    413.0000 P    8.183
1      1   CI_SLC   -1.2574   -0.0258   1164.0000 P   14.433
1      2   CI_SLP   -0.9276   -0.4863    113.0000 P   15.533
1      3   CI_SCD   -1.5184    0.1769    183.0000 P   15.923
1      4   CI_SXT   -1.5975    0.2555    488.0000 P   17.193
```

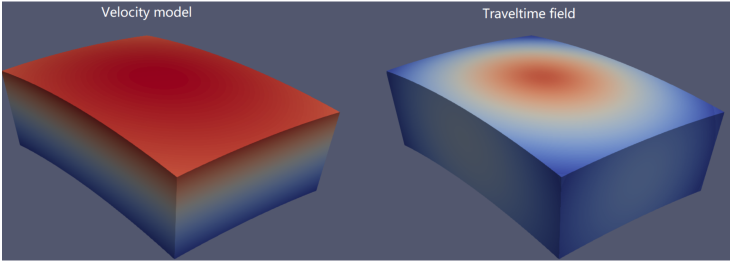

TomoATT

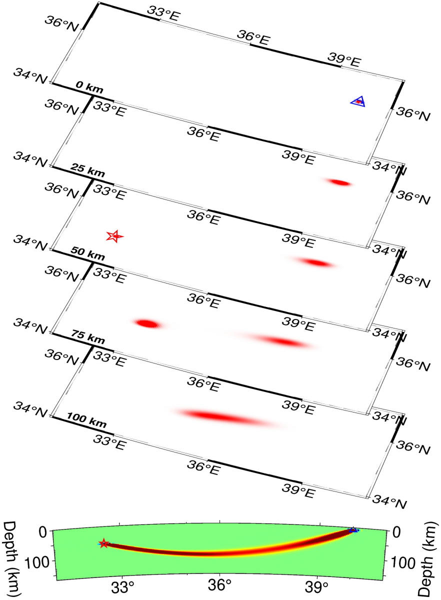

0 km
25 km
50 km
75 km
100 km
33°E
36°E
39°E
34°N
36°N
Depth (km)
0
100
33°
36°
39°

TomoATT

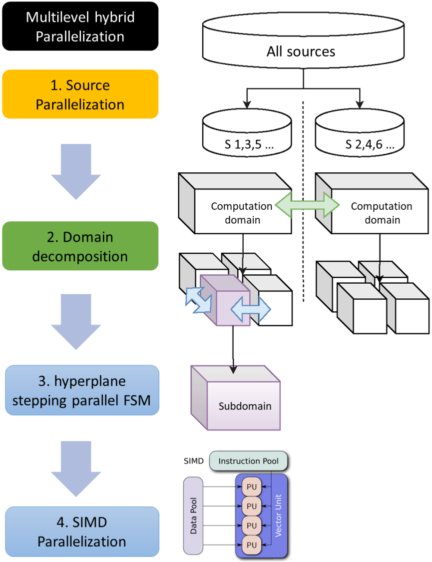
Multilevel hybrid Parallelization
1. Source Parallelization
2. Domain decomposition
3. hyperplane stepping parallel FSM
4. SIMD Parallelization
All sources
S 1,3,5 ...
S 2,4,6 ...
Computation domain
Computation domain
Subdomain
SIMD
Instruction Pool
Data Pool
PU
PU
PU
PU
Vector Unit

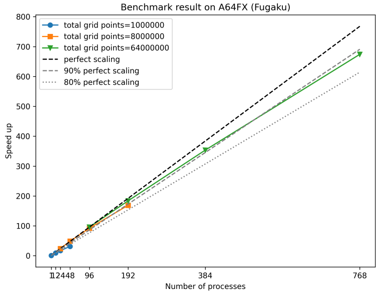
Benchmark result on A64FX (Fugaku)
total grid points=1000000
total grid points=8000000
total grid points=64000000
perfect scaling
90% perfect scaling
80% perfect scaling
Speed up
Number of processes
0
100
200
300
400
500
600
700
800
1
12
24
48
96
192
384
768

Software: SurfATT

SurfATT: Topography-incorporated surface wave traveltime tomography

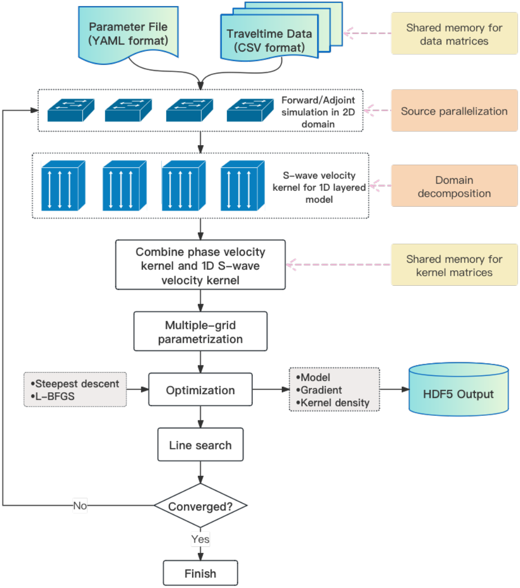

User-friendly

- Automatically fetches dependencies.
- Easily installable via CMake.
- Requires only 2 to 3 structured input files.
- Executed with just one command.

High-Performance

- Simultaneously processes multiple sources.
- Utilizes domain decomposition when computing sensitivity kernels.

Low Memory Cost

- Shared memory for data matrices.
- Shared memory for kernel matrices.

SurfATT: Topography-incorporated surface wave traveltime tomography

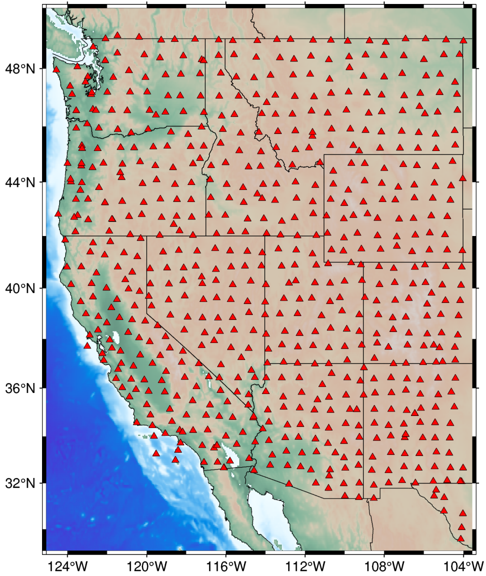

Case Example in the western United States

- Rayleigh wave phase-velocity database, 5–40 s, Ekström, G. (2014)
- 689 seismic stations, 7,454 virtual sources
- Grid size: $0.1^\circ \times 0.1^\circ \times 2$ km with 1,824,336 grid nodes
- Processors: 192. Intel Xeon Platinum 9242 Processor
- Elapsed time for 40 iterations: 00:14:28

Comparison with previous studies

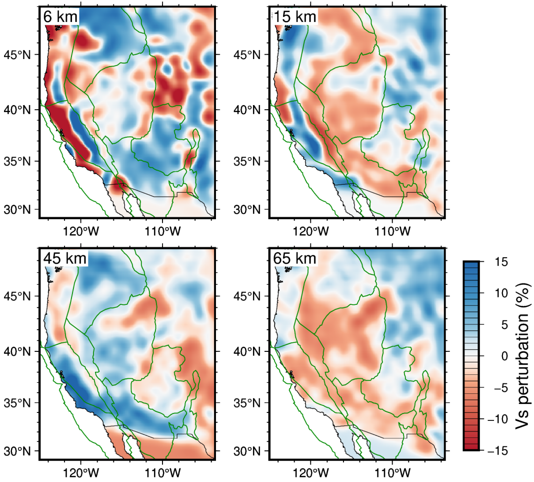

Yang et al., 2008, JGR: Solid Earth.

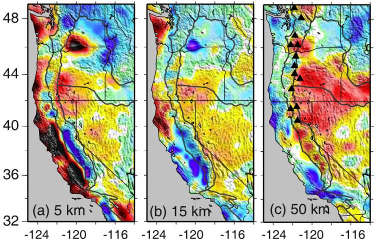

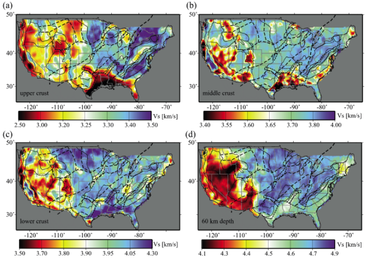

Schmandt et al., 2015, GRL.

III. Key Challenges in Imaging Transcrustal Magmatic Systems

Key Challenges in Imaging Transcrustal Magmatic Systems

P waves Only | P and PmP waves

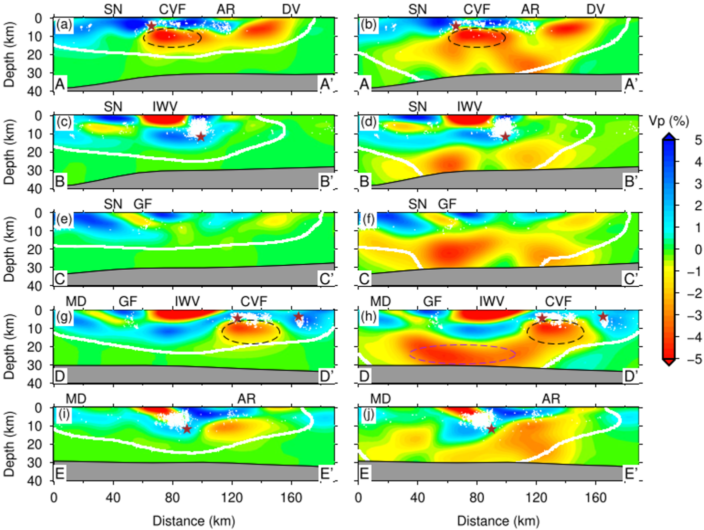

Key Challenges in Imaging Transcrustal Magmatic Systems

Limited Resolution in the Mid-Lower Crust

A central limitation arises from the restricted resolving power in the mid–lower crust, where seismic signals lose sensitivity to small melt fractions.

Other Limitations

- Non-uniqueness of seismic anomalies

  Low velocity can mean melt, fluids, hot rock, crystal-poor mush, or altered lithology — inversion alone cannot uniquely separate them.

- Poor constraints on melt fraction, geometry, and connectivity

  Even with a detected anomaly, imaging cannot easily tell if the system is a connected conduit, a mush zone, or isolated pockets.

PmP Waves to Enhance the Mid-lower Crust Resolution

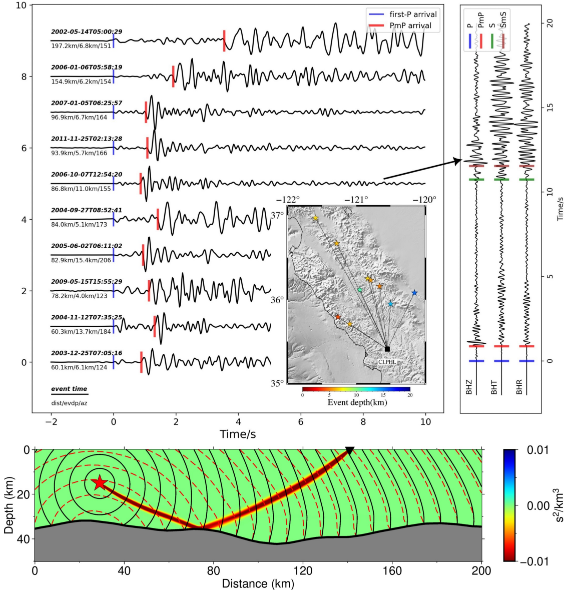

IV. PmPNet: a Machine Learning Tool for Picking Seismic PmP Waves

Seismic Conversions and Reflections

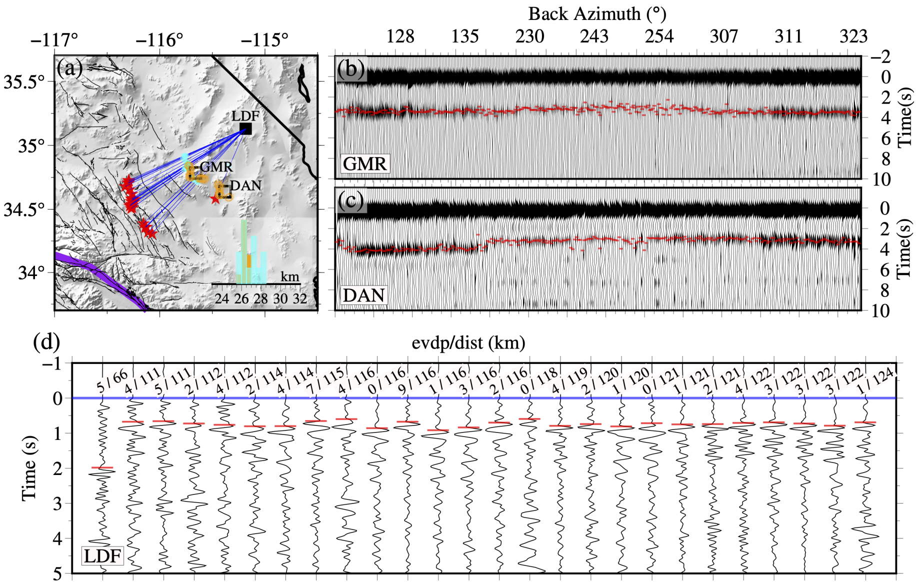

Seismic Data: Direct Waves and Reflections

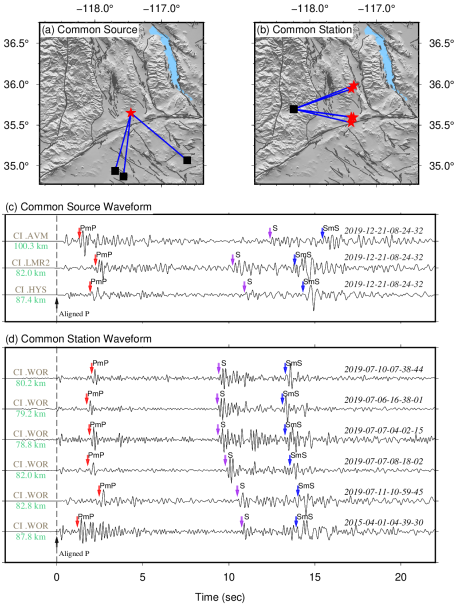

Southern California: Clear P, PmP, S and SmS waves

It is highly necessary to use high-frequency seismic phase information!

A long way ahead for full waveform inversion to use high-frequency seismic data

PmP Picking

PmP Picking

Stage I

Aligning seismic waveforms at the P-wave arrivals

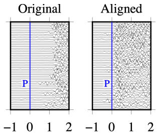

Searching for the PmP waves in a series of modified HK models

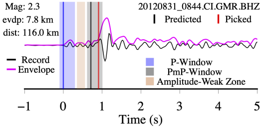

Retaining those three-component waveforms with identifiable P, PmP, S and SmS waves

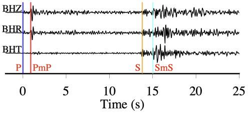

Stage II

Expanding the volumn of PmP dataset

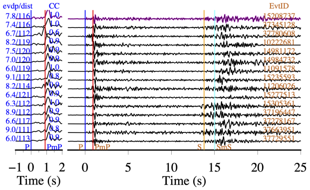

PmPNet

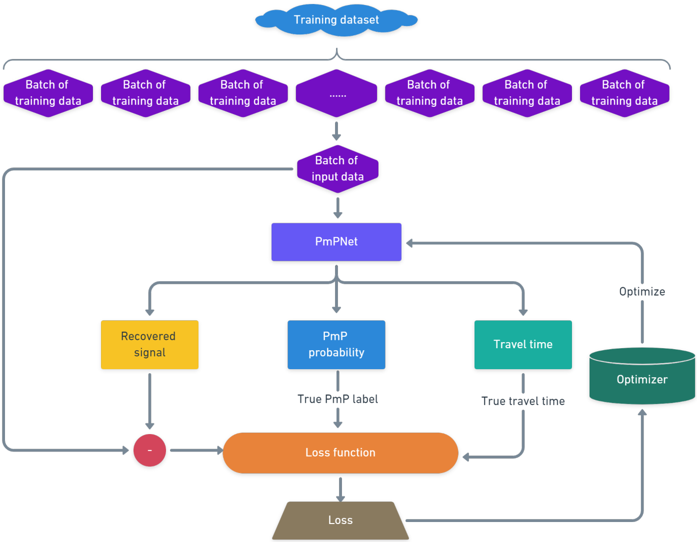
Training dataset
Batch of training data
Batch of training data
Batch of training data
......
Batch of training data
Batch of training data
Batch of training data
Batch of input data
PmPNet
Optimize
Recovered signal
PmP probability
Travel time
Optimizer
True PmP label
True travel time
-
Loss function
Loss

More PmP phases

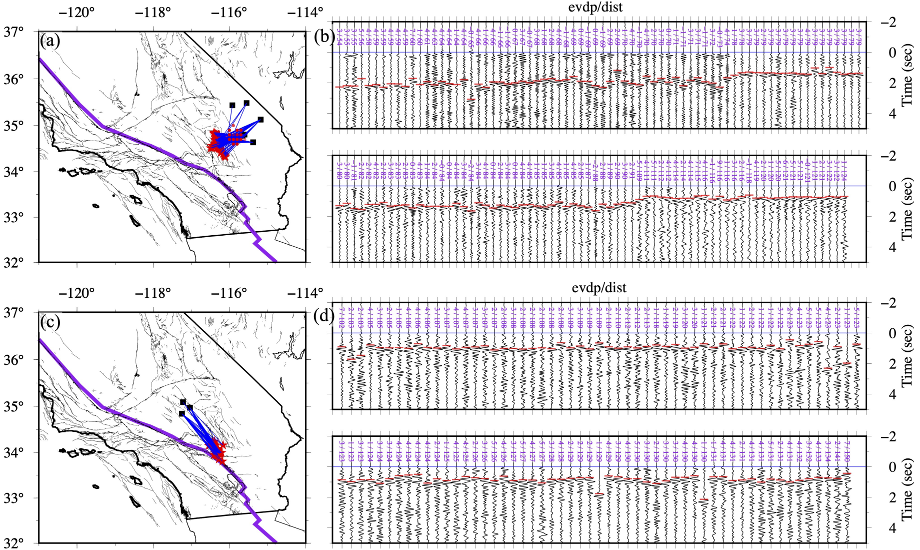

PNAS RESEARCH ARTICLE | EARTH, ATMOSPHERIC, AND PLANETARY SCIENCES

Check for updates

Multilevel transcrustal magmatic system beneath the Geysers-Clear Lake area

Tianjue Li[a,b], Shucheng Wu[a,b], and Ping Tong[a,b,c,1]

Edited by Michael Manga, University of California, Berkeley, CA; received October 13, 2023; accepted January 28, 2024

Magmatism in the Quaternary Clear Lake volcanic field (CLVF), with its youngest eruption having only occurred c. 10 ka ago, is commonly invoked as the heat source for the world's largest commercial geothermal reservoir, The Geysers, in northern California. A shallow silicic magma reservoir in the upper-middle crust has been discovered for some time, but the location and mechanism of a potential deep mafic magma reservoir have remained elusive. Here, we present a seismic tomographic model that images the entire crustal column, clearly revealing a multilevel transcrustal magmatic system beneath the Geysers-Clear Lake area. Upwelling melts from the mantle traverse across the crust-mantle boundary and accumulate in the lower crust underneath the southeastern part of Clear Lake, resulting in a hot Moho in between. Mafic melts primarily ascend westward due to the extensional regime in the west and physical barrier effect from the overlying rigid ophiolite fragment, ultimately forming a shallow silicic magma reservoir underlying and heating The Geysers geothermal field. In addition, this study also links compositionally diverse volcanism in a continental setting to differentiation in a multilevel transcrustal magmatic system.

Significance

Petrological and geochemical studies of the volcanic deposits and crustal xenoliths contained therein generally provide the fundamental knowledge of the underground magmatic systems in the past. Geophysical imaging instead imposes quantitative constraints on the present underground volumetric structures typically at a resolution of tens of kilometers.

Seismic imaging of the Clear Lake Volcanic Field

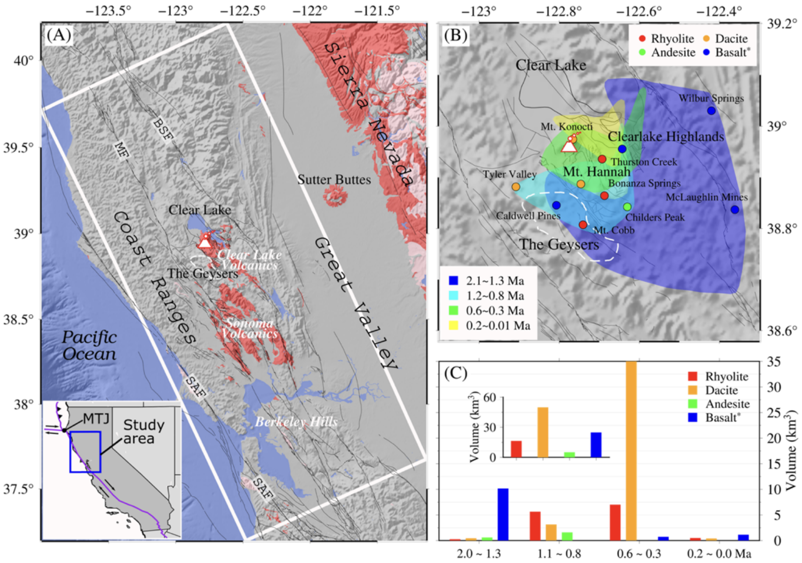

Seismic imaging of the Clear Lake Volcanic Field

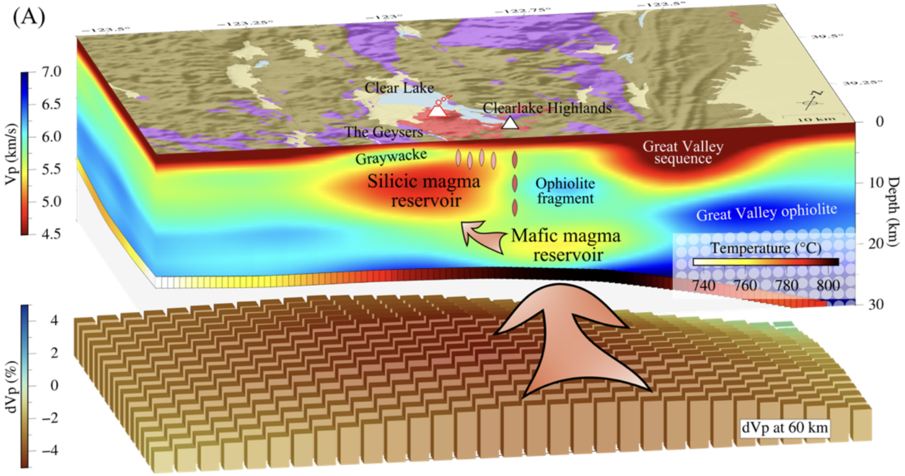

Part V: Our Studies of Geothermal Energy Potential in Singapore and Indonesia

Geothermal Reservoir Discovered in Singapore

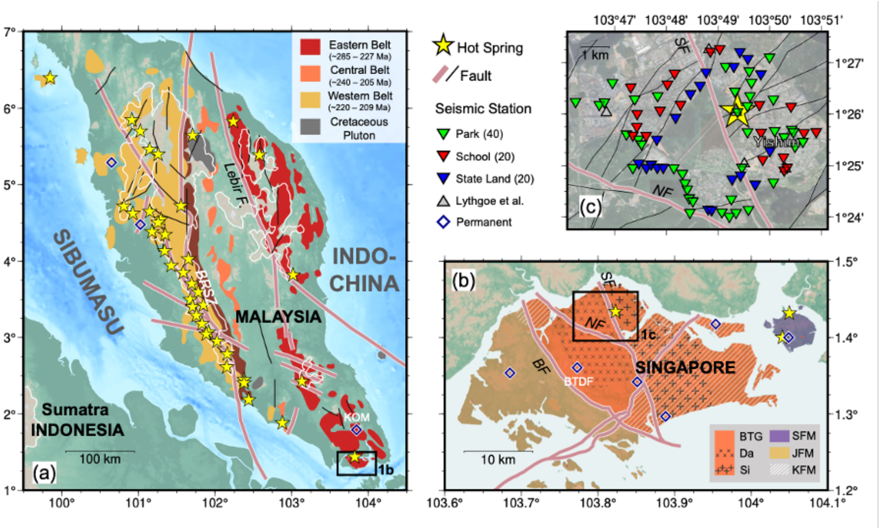

Geothermal Reservoir Discovered in Singapore

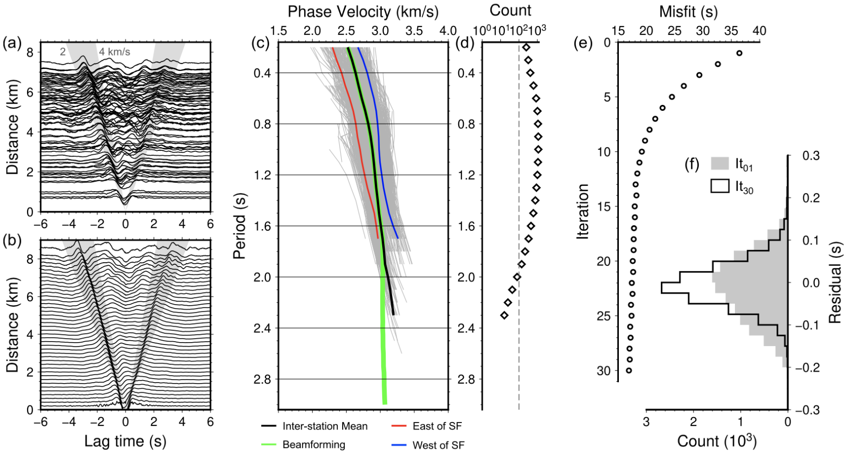

Geothermal Reservoir Discovered in Singapore

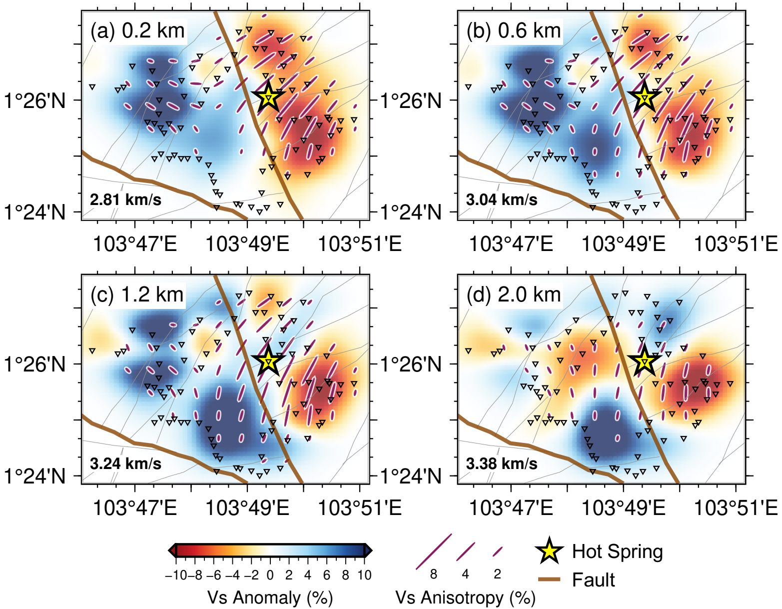

Geothermal Reservoir Discovered in Singapore

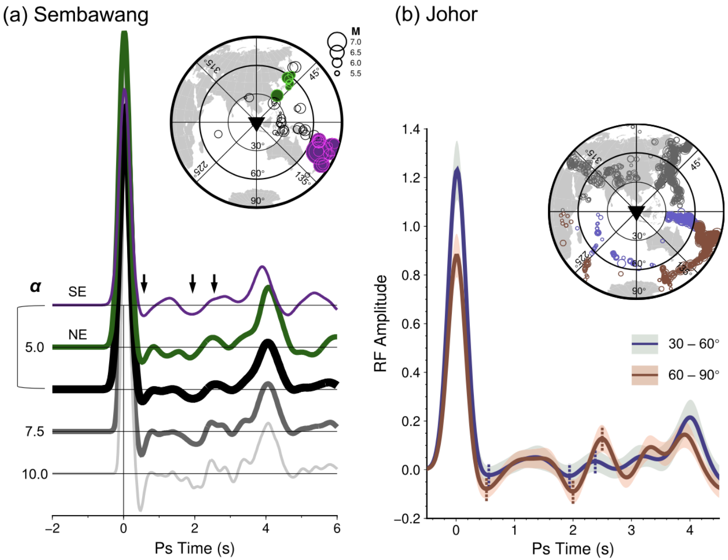

Geothermal Reservoir Discovered in Singapore

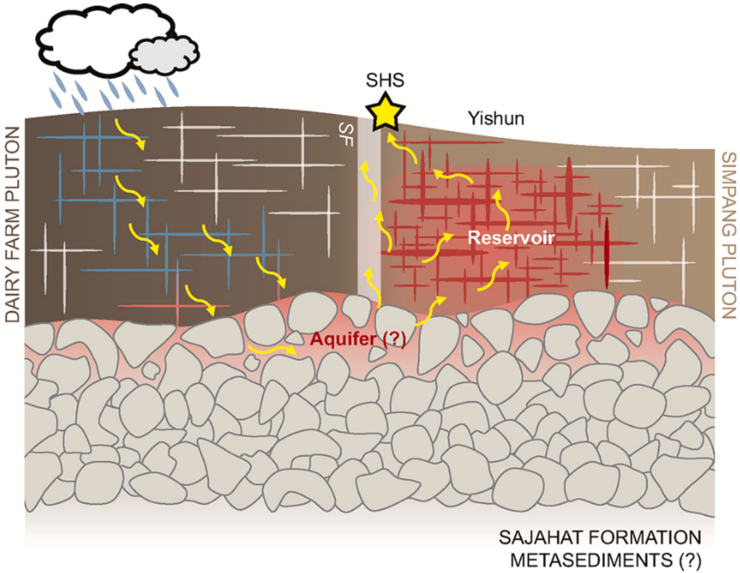

Engineering Geology 348 (2025) 107968

Contents lists available at ScienceDirect

Engineering Geology

journal homepage: www.elsevier.com/locate/enggeo

Geothermal potential in Singapore explored with non-invasive seismic data

Yiming Bai [a], Shijie Hao [a], Jinyun Xie [a,b,1], Mijian Xu [a,1], Xiao Xiao [a], Jing Chen [a], Chun Fei Chey [a], Dongdong Wang [a], Ping Tong [a,c,*]

[a] Division of Mathematical Sciences, School of Physical and Mathematical Sciences, Nanyang Technological University, Singapore
[b] Hubei Subsurface Multi-scale Imaging Key Laboratory, School of Geophysics and Geomatics, China University of Geosciences, Wuhan, China
[c] Earth Observatory of Singapore, Nanyang Technological University, Singapore

ARTICLE INFO

Keywords:
Geothermal exploration
Hot spring
Upper crustal structure
Seismic imaging
Tomography
Singapore

ABSTRACT

Singapore is dedicated to developing geothermal resources to meet rising energy demand and achieve net-zero emissions by 2050. While above-average heat flow and local hot springs suggest high geothermal potential beneath Singapore, the associated deep thermal sources remain underexplored due to a limited understanding of the subsurface structure. Applying ambient noise tomography and converted/reflected body-wave imaging to new seismic data from North Singapore reveals a highly fractured, fluid-saturated shallow geothermal reservoir located southeast of the Sembawang Hot Spring in the Yishun district. This reservoir exhibits low *Vs* (< 3.2 km/s) and high *Vp/Vs* (> 2.1). At a greater depth of $\sim$4 km, a crustal seismic discontinuity indicates a transition from the upper Bukit Timah Granite to the porous metasedimentary basement, where a deep aquifer might form, supplying the shallow reservoir and, ultimately, the Sembawang Hot Spring through the fault and fracture system. Our results highlight Yishun as a potential site for deep drilling in future geothermal explorations, and more broadly, provide new insights into the deep heat sources of numerous medium-to-low enthalpy geothermal sites throughout the Southeast Asian batholiths.

Geothermal Energy Potential in Singapore

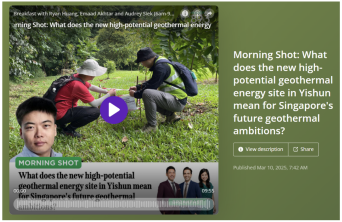

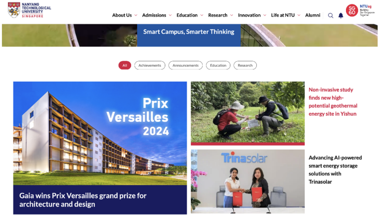

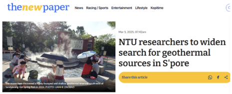

Continuation

Geothermal Energy Potential Exploration in Singapore

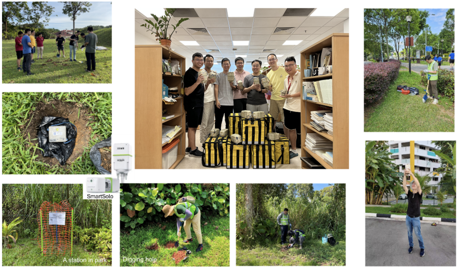

- **Start in January 2025,**
- **~S$0.7 million**

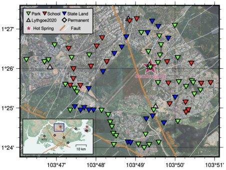

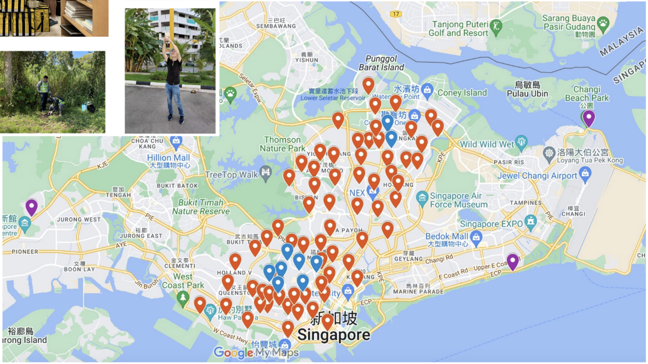

Geothermal Energy Exploration in Central Java

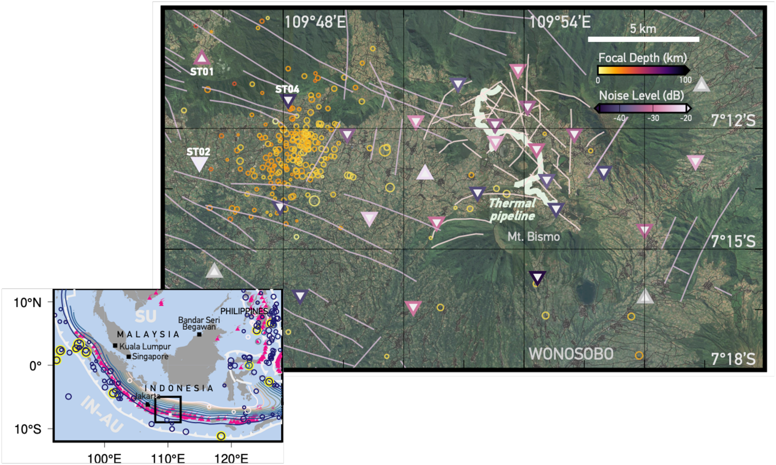

The Dieng Geothermal Power Plant is a 10 MW small-scale geothermal plant located on the Dieng Plateau in Central Java, Indonesia, which began operations in April 2021.

Geothermal Energy Exploration in Central Java

Geothermal Energy Exploration in Central Java

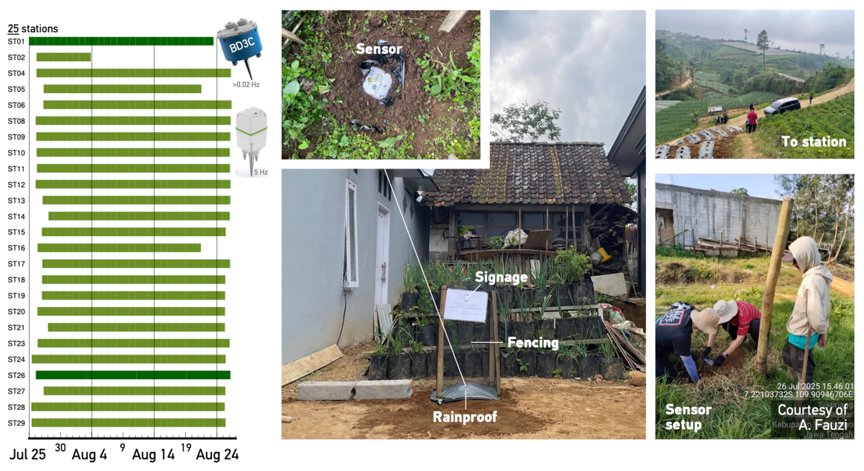

Geothermal Energy Exploration in Central Java

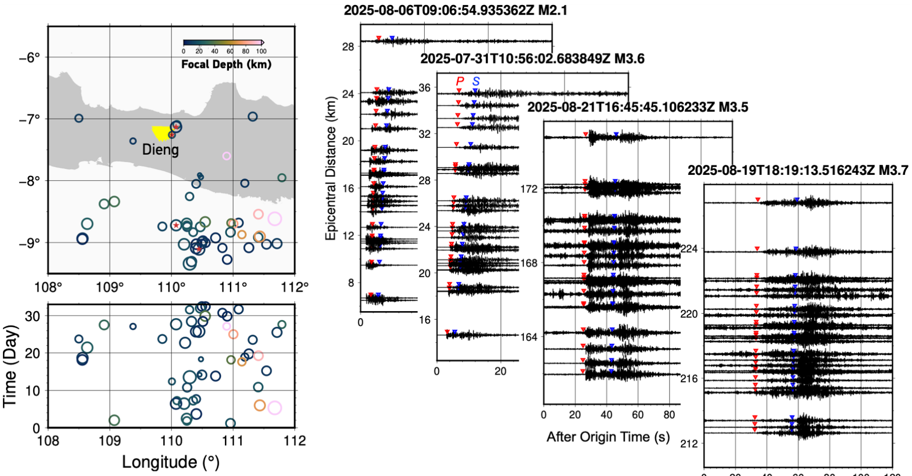

Geothermal Energy Exploration in Central Java

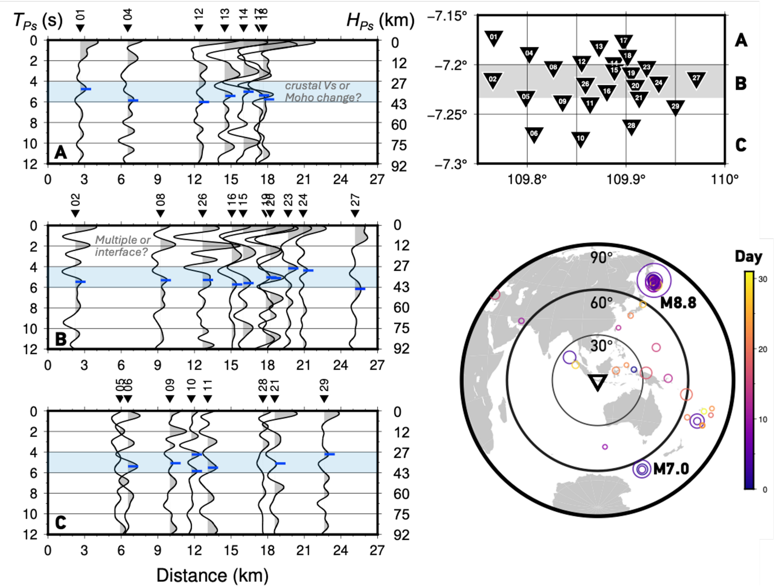

Remarks

- TomoATT and SurfATT offer precise and reliable tomographic results, utilizing various data types to explore multi-scale subsurface structures.
- You are encouraged to employ TomoATT and SurfATT when inverting travel time data to deduce velocity heterogeneity, seismic anisotropy, and attenuation mdoels.
- Comprehensive guidelines will be provided.

VI: Theoretical Foundation of Adjoint-State Traveltime Tomography

Theoretical Foundation

A. Physical Models for Seismic Traveltime
B. Source-Receiver Geometry
C. Objective Functions for Traveltime Tomography
D. Fréchet Derivatives and Sensitivity Kernels
E. Model Parameterization
F. Iterative Inversion
G. Forward Numerical Solvers
H. Regularization

A. Physical Models for Seismic Traveltime

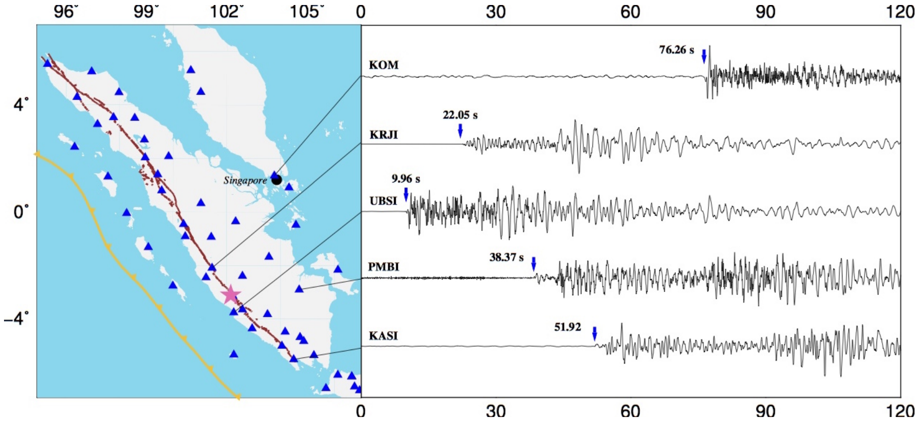

- Traveltime is the most robust information that can be extracted from seismic records.

A. Physical Models for Seismic Traveltime

The elliptical anisotropic eikonal equation

$$\begin{cases} \sqrt{[\nabla T(\mathbf{x})]^t \, M(\mathbf{x}) \nabla T(\mathbf{x})} = 1, \quad \mathbf{x} \in \Omega \setminus \{\mathbf{x}_s\}, \\ T(\mathbf{x}_s) = 0. \end{cases} \tag{3}$$

Ω the Earth volume; $T(\mathbf{x})$ traveltime filed; $\mathbf{x}_s$ source location; $M(\mathbf{x})$ a symmetric positive definite matrix describing material properties (Luo and Qian 2012).

Isotropic:

$$M(\mathbf{x}) = \frac{1}{s^2(\mathbf{x})} \begin{bmatrix} 1 & 0 & 0 \\ 0 & 1 & 0 \\ 0 & 0 & 1 \end{bmatrix} \tag{4}$$

A. Physical Models for Seismic Traveltime

Radially Anisotropic (VTI):

$$M(\mathbf{x}) = \frac{1}{s^2(\mathbf{x})} \begin{bmatrix} 1+2\xi(\mathbf{x}) & 0 & 0 \\ 0 & 1+2\xi(\mathbf{x}) & 0 \\ 0 & 0 & 1-2\xi(\mathbf{x}) \end{bmatrix} \tag{5}$$

Azimuthally Anisotropic:

$$M(\mathbf{x}) = \frac{1}{s^2(\mathbf{x})} \begin{bmatrix} 1+2\xi(\mathbf{x}) & 2\eta(\mathbf{x}) & 0 \\ 2\eta(\mathbf{x}) & 1-2\xi(\mathbf{x}) & 0 \\ 0 & 0 & 1 \end{bmatrix} \tag{6}$$

B. Source-Receiver Geometry

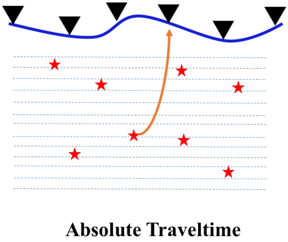

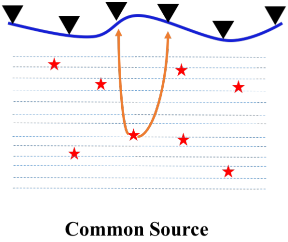

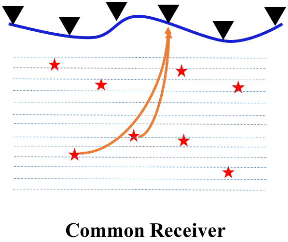

N earthquakes $\mathbf{x}_{s,n}$ $(n = 1, 2, \cdots, N)$; L seismic stations $\mathbf{x}_{r,l}$ $(l = 1, 2, \cdots, L)$; $T_n(\mathbf{x})$ calculated traveltime field of the first P- or S-wave arrival emanating from $\mathbf{x}_{s,n}$; $T_n^o(\mathbf{x}_{r,k})$ observed traveltime.

- Absolute traveltime: $T_n^o(\mathbf{x}_{r,l})$
- Common-source double difference: $T_n^o(\mathbf{x}_{r,j}) - T_n^o(\mathbf{x}_{r,k})$
- Common-receiver double difference: $T_n^o(\mathbf{x}_{r,l}) - T_k^o(\mathbf{x}_{r,l})$

C. Objective Functions for Traveltime Tomography

Absolute traveltime tomography:

$$\chi\left(M(\mathbf{x})\right) = \sum_{n=1}^{N}\sum_{l=1}^{L}\frac{\omega_{n,l}}{2}\left[T_n(\mathbf{x}_{r,l}) - T_n^o(\mathbf{x}_{r,l})\right]^2 , \tag{7}$$

Common-source double-difference traveltime tomography:

$$\chi\left(M(\mathbf{x})\right) = \sum_{j=1}^{L}\sum_{k=1}^{L}\sum_{n=1}^{N}\frac{\omega_{j,k}^{n}}{2}\left\{\left[T_n(\mathbf{x}_{r,j}) - T_n(\mathbf{x}_{r,k})\right] - \left[T_n^o(\mathbf{x}_{r,j}) - T_n^o(\mathbf{x}_{r,k})\right]\right\}^2 . \tag{8}$$

Common-receiver double-difference traveltime tomography:

$$\chi\left(M(\mathbf{x})\right) = \sum_{n=1}^{N}\sum_{k=1}^{N}\sum_{l=1}^{L}\frac{\omega_{n,k}^{l}}{2}\left\{\left[T_n(\mathbf{x}_{r,l}) - T_k(\mathbf{x}_{r,l})\right] - \left[T_n^o(\mathbf{x}_{r,l}) - T_k^o(\mathbf{x}_{r,l})\right]\right\}^2 . \tag{9}$$

D. Fréchet Derivatives and Sensitivity Kernels

Absolute traveltime tomography (for isotropic media)

$$\delta\chi\left(M(\mathbf{x})\right) = \int_{\Omega} K_s(\mathbf{x}) \frac{\delta s(\mathbf{x})}{s(\mathbf{x})} d\mathbf{x}, \tag{10}$$

where

$$K_s(\mathbf{x}) = \sum_{n=1}^{N} P_n(\mathbf{x}) s^2(\mathbf{x}), \tag{11}$$

and $P_n(\mathbf{x})$ is called the adjoint traveltime field, satisfying

$$\begin{cases} \nabla \cdot \left[P_n(\mathbf{x}) \nabla \left(-T_n(\mathbf{x})\right)\right] = \sum_{l=1}^{L} \omega_{n,l} \left[T_n(\mathbf{x}) - T_n^o(\mathbf{x}_{r,l})\right] \delta(\mathbf{x} - \mathbf{x}_{r,l}), & x \in \Omega \\ P_n(\mathbf{x}) = 0, & \mathbf{x} \in \partial\Omega. \end{cases} \tag{12}$$

D. Fréchet Derivatives and Sensitivity Kernels

Absolute traveltime tomography (for isotropic media)

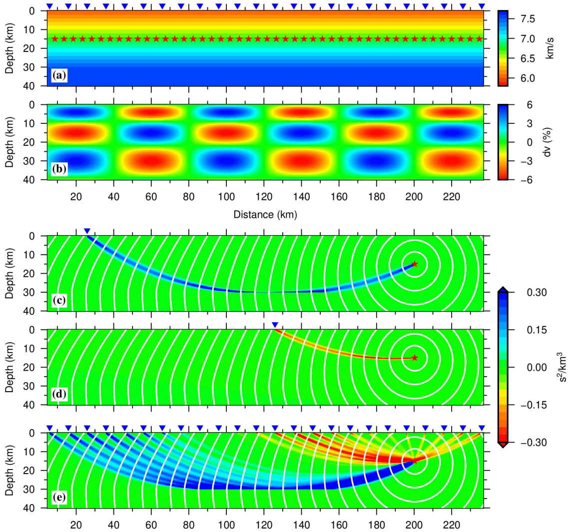

D. Fréchet Derivatives and Sensitivity Kernels

Common-source double-difference traveltime tomography

$$\delta\chi\left(M(\mathbf{x})\right) = \int_\Omega K_s(\mathbf{x}) \frac{\delta s(\mathbf{x})}{s(\mathbf{x})} d\mathbf{x}, \tag{13}$$

where

$$K_s(\mathbf{x}) = \sum_{n=1}^{N} P_n(\mathbf{x}) s^2(\mathbf{x}), \tag{14}$$

and $P_n(\mathbf{x})$ is the adjoint field satisfying $P_n(\mathbf{x}) = 0$ on $\partial\Omega$

$$\begin{aligned} &\nabla \cdot \left[P_n(\mathbf{x}) \nabla(-T_n(\mathbf{x}))\right] \\ =& \sum_{j=1}^{L}\sum_{k=1}^{L} 2\omega_{j,k}^{n} \left\{\left[T_n(\mathbf{x}) - T_n(\mathbf{x}_{r,k})\right] - \left[T_n^o(\mathbf{x}) - T_n^o(\mathbf{x}_{r,k})\right]\right\} \delta(\mathbf{x} - \mathbf{x}_{r,j}). \end{aligned} \tag{15}$$

D. Fréchet Derivatives and Sensitivity Kernels

Common-source double-difference traveltime tomography

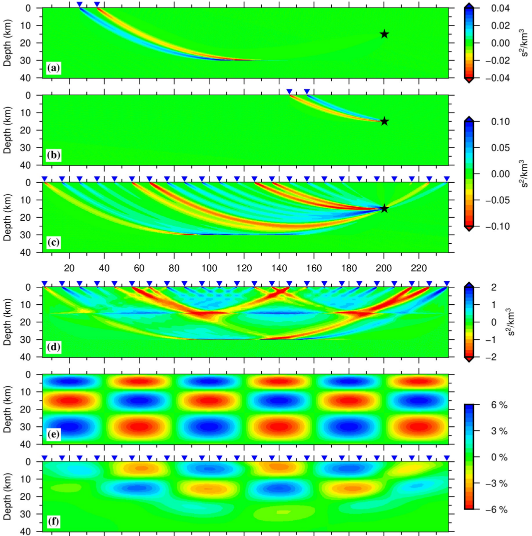

D. Fréchet Derivatives and Sensitivity Kernels

Common-receiver double-difference traveltime tomography

$$\delta\chi\left(s(\mathbf{x})\right) = \int_{\Omega} K_s(\mathbf{x}) \frac{\delta s(\mathbf{x})}{s(\mathbf{x})} d\mathbf{x}, \tag{16}$$

where

$$K_s(\mathbf{x}) = \sum_{n=1}^{N} 2P_n(\mathbf{x}) s^2(\mathbf{x}). \tag{17}$$

and $P_n(\mathbf{x})$ is the adjoint field satisfying $P_n(\mathbf{x}) = 0$ on $\partial\Omega$

$$\nabla \cdot [P_n(\mathbf{x}) \nabla(-T_n(\mathbf{x}))] = \sum_{k=1}^{N} \sum_{l=1}^{L} \omega_{n,k}^{l} \{[T_n(\mathbf{x}) - T_k(\mathbf{x})] - [T_n^o(\mathbf{x}) - T_k^o(\mathbf{x})]\} \delta(\mathbf{x} - \mathbf{x}_{r,l}) \tag{18}$$

D. Fréchet Derivatives and Sensitivity Kernels

Common-receiver double-difference traveltime tomography

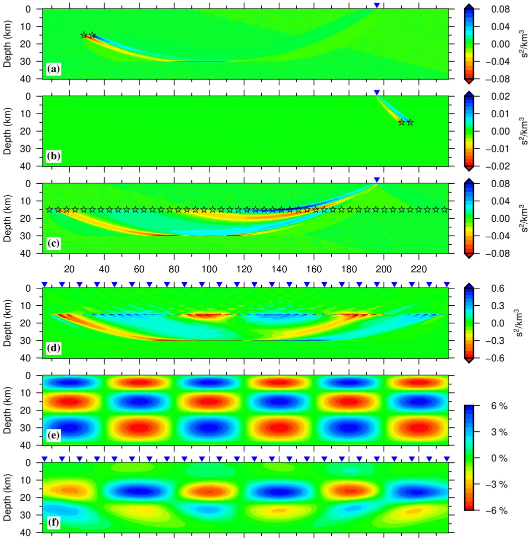

D. Fréchet Derivatives and Sensitivity Kernels

Azimuthally anisotropic tomography

$$\delta\chi\left(M(\mathbf{x})\right) = \int_\Omega K_s(\mathbf{x})\frac{\delta s(\mathbf{x})}{s(\mathbf{x})}d\mathbf{x} + \int_\Omega K_\xi(\mathbf{x})\delta\xi(\mathbf{x})d\mathbf{x} + \int_\Omega K_\eta(\mathbf{x})\delta\eta(\mathbf{x})d\mathbf{x}, \tag{19}$$

where

$$K_s(\mathbf{x}) = \sum_{n=1}^{N} P_n(\mathbf{x})s^2(\mathbf{x}), \tag{20}$$

$$K_\xi(\mathbf{x}) = \sum_{n=1}^{N} \left[\nabla T_n(\mathbf{x})\right]^t \begin{bmatrix} -1 & 0 & 0 \\ 0 & 1 & 0 \\ 0 & 0 & 0 \end{bmatrix} \nabla T_n(\mathbf{x})P_n(\mathbf{x}), \tag{21}$$

D. Fréchet Derivatives and Sensitivity Kernels

Azimuthally anisotropic tomography (continued)

$$K_\eta(\mathbf{x}) = \sum_{n=1}^{N} [\nabla T_n(\mathbf{x})]^t \begin{bmatrix} 0 & -1 & 0 \\ -1 & 0 & 0 \\ 0 & 0 & 0 \end{bmatrix} \nabla T_n(\mathbf{x}) P_n(\mathbf{x}). \tag{22}$$

$P_n(\mathbf{x})$ is the adjoint field satisfying $P_n(\mathbf{x}) = 0$ on $\partial\Omega$ and

$$\begin{aligned} &\nabla \cdot \left\{ P_n(\mathbf{x}) \left[-\nabla T_n(\mathbf{x})\right]^t \begin{bmatrix} 1+2\xi(\mathbf{x}) & 2\eta(\mathbf{x}) & 0 \\ 2\eta(\mathbf{x}) & 1-2\xi(\mathbf{x}) & 0 \\ 0 & 0 & 1 \end{bmatrix} \right\} \\ &= \sum_{m=1}^{M} \omega_{n,m} \left[T_n(\mathbf{x}) - T_n^o(\mathbf{x}_{r,m})\right] \delta(\mathbf{x} - \mathbf{x}_{r,m}), \quad \mathbf{x} \in \Omega \setminus \{\mathbf{x}_s\}. \end{aligned} \tag{23}$$

D. Fréchet Derivatives and Sensitivity Kernels

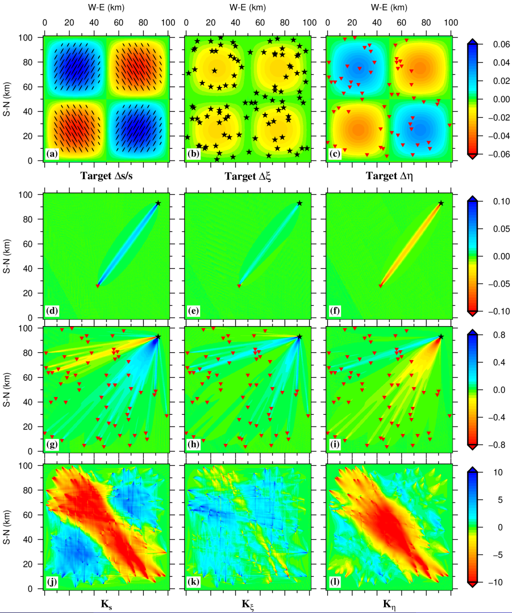

E. Model Parameterization

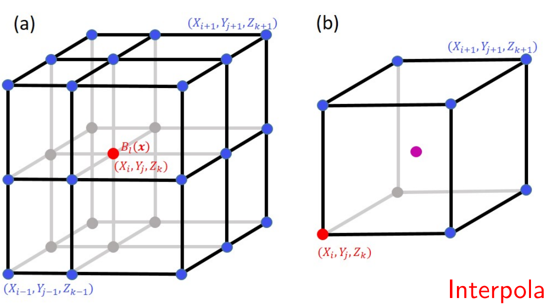

$$\delta\chi\left(s(\mathbf{x})\right) = \int_{\Omega} K_s(\mathbf{x}) \frac{\delta s(\mathbf{x})}{s(\mathbf{x})} d\mathbf{x}$$

Define one basis function at each node

$$\frac{\delta s(\mathbf{x})}{s(\mathbf{x})} = \sum_{l=1}^{L} \delta C_l B_l(\mathbf{x})$$

Interpolate on multiple regular grids

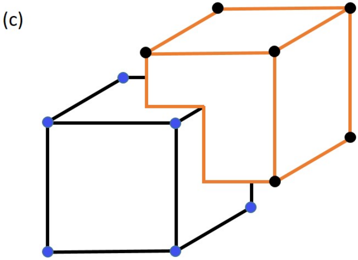

$$\frac{\delta s(\mathbf{x})}{s(\mathbf{x})} = \frac{1}{H} \sum_{h=1}^{H} \sum_{l=1}^{L_h} \delta C_{l,h} B_{l,h}(\mathbf{x})$$

The derivative of $\chi\left(s(\mathbf{x})\right)$ with respect to the node parameter $C_{l,h}$,

$$\frac{\partial \chi\left(s(\mathbf{x})\right)}{\partial C_{l,h}} = \frac{1}{H} \int_{\Omega} K_s(\mathbf{x}) B_{l,h}(\mathbf{x}) d\mathbf{x}.$$

F. Iterative Inversion

The step-size-controlled gradient descent method to iteratively find the minimum of the objective function $\chi(s(\mathbf{x})) = \chi(C_{1,1}, C_{2,1}, \cdots, C_{L_H,H})$

Let $\mathbf{X} = (C_{1,1}, C_{2,1}, \cdots, C_{L_H,H})$ and set an upper bound γ for the L_1 norm of its perturbation $||\Delta\mathbf{X}||_1$ at every iteration (Damping regularization). The algorithm is given below, which starts from $k = 0$ and $\mathbf{X}^0 = \mathbf{0}$.

1. Compute the objective function $\chi(\mathbf{X}^k)$ and gradient vector $\mathbf{g}^k = \partial\chi/\partial\mathbf{X}^k$. When $k > 0$, divide the upper bound γ by a factor of $\kappa > 1$ as $\gamma \to \gamma/\kappa$ if $\chi(\mathbf{X}^k) > \chi(\mathbf{X}^{k-1})$.
2. Let $f = \chi(\mathbf{X}^k)$ and $g = \mathbf{g}^k \cdot \mathbf{g}^k$, compute the step size $\lambda_k = f/(2g)$.
3. Compute $\alpha_k = \gamma/||\lambda_k\mathbf{g}^k||_1$ if $||\lambda_k\mathbf{g}^k||_1 > \gamma$, otherwise $\alpha_k = 1$.
4. Compute $\Delta\mathbf{X} = -\alpha_k\lambda_k\mathbf{g}^k$, and update the model $\mathbf{X}^{k+1} = \mathbf{X}^k + \Delta\mathbf{X}$.
5. If $g \leq \epsilon$, the tolerance level, or k exceeds the pre-defined maximum iteration number, or the objective function value becomes stable as $|\chi(\mathbf{X}^k) - \chi(\mathbf{X}^{k-1})|/\chi(\mathbf{X}^0) \leq \theta$ (θ is relatively small), then $\mathbf{X}^{k+1}$ is the optimal solution; otherwise go back to the first step with $k+1$.

G. Forward Solvers

Eikonal equation: Fast sweeping method (Zhao, 2004; Qian et al., 2007)

$$\begin{cases} \sqrt{[\nabla T(\mathbf{x})]^t M(\mathbf{x}) \nabla T(\mathbf{x})} = 1, \quad \mathbf{x} \in \Omega \setminus \{\mathbf{x}_s\}, \\ T(\mathbf{x}_s) = 0. \end{cases}$$

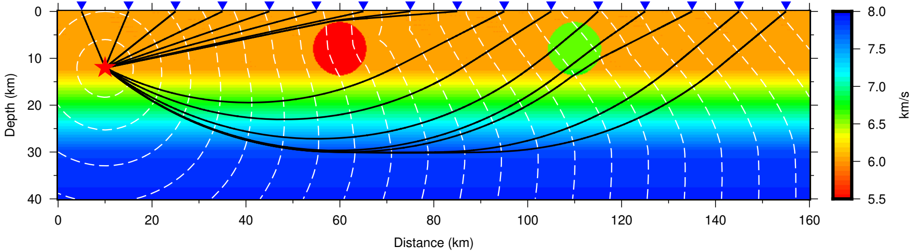

It is more challenging to solve an anisotropic eikonal equation than its isotropic counterpart.

G. Forward Solvers

Adjoint equation: Fast sweeping method (Leung and Qian, 2006)

$$\begin{cases} \nabla \cdot \left[P_n(\mathbf{x})\nabla\left(-T_n(\mathbf{x})\right)\right] = \sum_{l=1}^{L} f_l(\mathbf{x})\delta(\mathbf{x}-\mathbf{x}_{r,l}), & x \in \Omega \\ P_n(\mathbf{x}) = 0, & \mathbf{x} \in \partial\Omega. \end{cases}$$

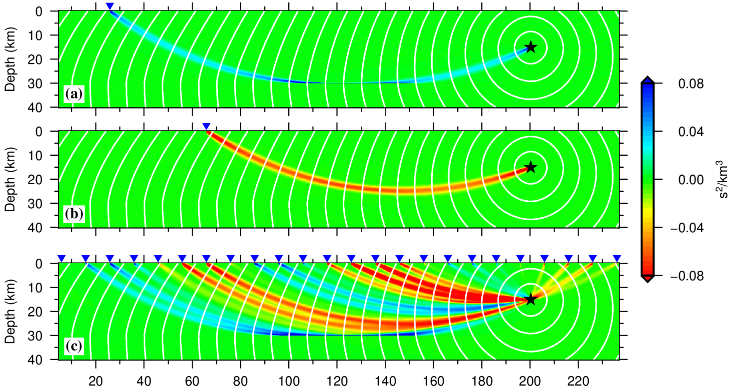

H. Regularization

Damping

Implicitly implemented via the step-size-controlled gradient descent method. At each iteration, the maximum perturbation is restricted within $\pm 2.0\%$, equivalent to applying the optimal damping parameter

Smoothing

Implicitly implemented via the coarse inversion grid (multiple-grid model parameterization).

The spacing of the inversion grid is adjusted based on the resolution scale of the using data. Checkerboard resolution tests can be performed to choose a proper multiple-grid.

References

- Tong, P., 2021. Adjoint-state traveltime tomography for azimuthally anisotropic media and insight into the crustal structure of central California near Parkfield, Journal of Geophysical Research: Solid Earth, 126, e2021JB022365.
- Tong, P., 2021. Adjoint-state traveltime tomography: Eikonal equation-based methods and application to the Anza area in southern California, Journal of Geophysical Research: Solid Earth, 126, e2021JB021818.
- Liu, Y., Tong, P., 2021. Eikonal equation-based P-wave seismic azimuthal anisotropy tomography of the crustal structure beneath northern California, Geophysical Journal International, 226(1), 287-301.
- Ding, W., Li, T., Yang, X., Ren, K., Tong, P., 2022. Deep neural networks for creating reliable PmP database with a case study in southern California, Journal of Geophysical Research: Solid Earth, 127(4), e2021JB023830.

References

- Li, T., Yao, J., Wu, S., Xu, M., Tong, P., 2022. Moho complexity in southern California revealed by local PmP and teleseismic Pms waves, Journal of Geophysical Research: Solid Earth, 127(2), e2021JB023033.
- Yao, J., Wu. S., Li, T., Xiao, X., Hubbard, J., Wang, Y., Thant, M., Tong, P., 2022. Imaging the upper 10 km crustal shear-wave velocity structure of central Myanmar via a joint inversion of body-wave polarizations and receiver functions, Seismological Research Letters, 93(3), 1710-1720.
- Chen, J., Chen. G., Wu, H., Yao, J., Tong, P., 2022. Adjoint tomography of northeast Japan revealed by common-source double-difference traveltime data, Seismological Research Letters, 93(3), 1835-1851.
- Wang, D., Wu, S., Li, T., Tong, P., Gao, Y., 2022. Elongated magma plumbing system beneath the Coso volcanic field, California, constrained by seismic reflection tomography, Journal of Geophysical Research: Solid Earth, 127(6), e2021JB023582.